J Inf Process Syst, Vol.19, No.2, pp.173~188, April 2023
https://doi.org/10.3745/JIPS.04.0270

ISSN 1976-913X (Print)
ISSN 2092-805X (Electronic)

JOURNAL OF INFORMATION PROCESSING SYSTEMS JIPS

High Shock-Resistant Design of Piezoresistive High-g Accelerometer

Yongle Lu*, Zhen Qu, Jie Yang, Wenxin Wang, Wenbo Wang, and Yu Liu

Abstract

To improve the shock-resistance of piezoresistive high-g accelerometer, we propose a design of piezoresistive high-g accelerometer. The accelerometer employs special-shaped proof masses system with a cross gap. Four tiny sensing beams are bonded above the cross gap. The expression of the deformation, natural frequency and damping is deduced, and the structural parameters are optimized. The accelerometer structure is simulated and verified by finite element method (FEM) simulation. The results show that the range of the accelerometer can reach 200,000 g, the natural frequency is 453.6 kHz, and the cross-axis sensitivity of X-axis and Y-axis is 0.25% and 0.11%, respectively, which can apply to the measurement of high shock. Contrastively, the cross-axis sensitivity of X-axis and Y-axis is respectively, reduced by 93.2% and 96.9%. The sensitivity of our accelerometer is 0.88 μV/g. It is of great value for the application of piezoresistive high-g accelerometer with high shock-resistance.

Keywords

FEM, High-g Accelerometer, Natural Frequency, Piezoresistive, Transverse Effect

1. Introduction

High-g accelerometer is one of the important components on impact, which has been used in automotive airbags [1,2], military weapons [3], industrial production [4] and other harsh environments [5-7]. Of them, piezoresistive high-g accelerometer is based on the effect of stress on electrical properties, which is essentially from displacement of the spring-mass system [8]. It is widely used in high-g measurement of civil or military field because of the characteristics of simple signal processing circuits [9], strong resistance to impact [10], low cost [11], and so on.

The application in high impact situations put forward higher requirements for the performance of high-g accelerometers. When designing high-g accelerometers, some researchers proposed novel structures or effective packaging method to ensure survival and accurate measurement of high-g accelerometers in harsh environments. In addition, some new materials or new fabrication processes are used to improve its performance [12]. An earlier record in 2009 showed that Atwell et al. [13] designed a piezoresistive high-g accelerometer using 6H-SiC. According to the high-g simulation, the accelerometer had a range above 100,000 g and a sensitivity up to 343 nV/g. Shi et al. [14] presented a novel piezoresistive high-g

Manuscript received November 16, 2021; first revision May 26, 2022; accepted July 8, 2022.

* **Corresponding Author:** Yongle Lu (luyl@cqupt.edu.cn)
School of Optoelectronic Engineering, Chongqing University of Post and Telecommunications, Chongqing, China (luyl@cqupt.edu.cn, 1421701967@qq.com, 2366673625@qq.com, 531155354@qq.com, s190431003@stu.cqupt.edu.cn, liuyu@cqupt.edu.cn)

accelerometer in 2018, which employed our-beams and central-island mass silicon structure. The sensitivity and the natural frequency of the accelerometer were 0.5611 μV/g and 408.19 kHz, respectively. The accelerometer had also shown stability in shock experiments. Their team proposed "high-solid-wave unloading" packaging method in 2020 [15]. In shock testing, the survival rate of the accelerometers with this packaging system was up to 100% and the measurement accuracy reached 95%. Jia et al. [16] proposed a piezoresistive shock accelerometer with four self-supporting beams to enhance sensitivity and natural frequency. The pure axial deformation can occur on its microbeams after dimensions optimization. The sensitivity of the shock accelerometer is 1.586 μV/g/3 V and the natural frequency is 445 kHz according to impact tests. In 2021, Jangra et al. [17] put forward a high-g Z-axis accelerometer with serpentine spring structure, which had high displacement sensitivity (approximately 357.68 nm/g). However, the transverse effect, one of the negative effects, is sometimes neglected in many studies of high-g accelerometer. The transverse effect will lead to the accelerometer damage due to rotation of the proof masses and it has a detrimental effect on the accuracy of measured value along sensing axis. We consider cross-axis sensitivity in the design of piezoresistive high-g accelerometer to optimize resistance to impact.

In this paper, a piezoresistive high-g accelerometer with special-shaped proof masses system with a cross gap is introduced. It has a measurement range of 200,000 g. Four tiny sensing beams are bonded above the cross gap, which can shorten the distance between the gravity center of the proof masses system and the neutral layer of supporting beams to restrain transverse effect. The tiny sensing beams can also weaken the compromise between natural frequency and sensitivity. Therefore, the accelerometer is optimized to improve shock-resistance.

This paper is organized as follows: Section 2 discusses the structure of accelerometer. In Section 3, we deduce the expression of the maximum deformation, natural frequency, and damping. In Section 4, we optimize the accelerometer by combining theory with simulation. In Section 5, we simulate and analyze the accelerometer characteristics to verify our design. Section 6 concludes this paper.

2. Structure Design of Accelerometer

The designed accelerometer structure is schematically shown in Fig. 1. It can be seen in Fig. 1(a) that the structure is composed of four tiny sensing beams, four proof masses, a supporting frame for proof masses, four supporting beams and an accelerometer frame. The upper surfaces of all structures lie in the same plane, making accelerometers easier to fabricate [15]. Fig. 1(b) shows that proof masses have great thick-ness compared with the tiny sensing beams. There is a certain distance between the structure and the bottom plate.

The sensitive direction of the proposed accelerometer is the axis Z, which is perpendicular to the surface of the accelerometer structure. The whole structure is symmetric about the center of the plane XOY, and the two supporting beams are symmetrically distributed along the direction of the axis X and Y, respectively. Preliminarily, the accelerometer uses silicon as the main material and uses glass as a bottom floor.

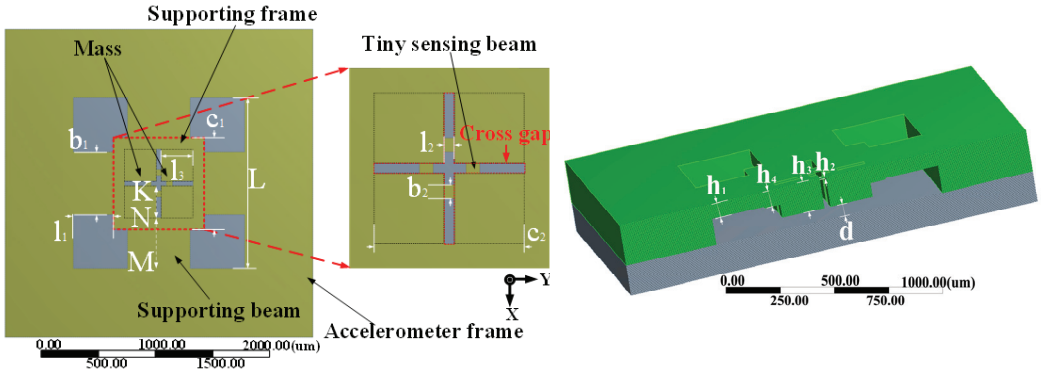

(a) (b)

Fig. 1. (a) The accelerometer structure is composed of four tiny sensing beams, four proof masses, supporting frame for proof masses, four supporting beams and an accelerometer frame. The upper surfaces of all structures lie in the same plane. There is a cross gap between four proof masses. (b) The accelerometer includes an accelerometer structure and a bottom floor. The distance between the proof masses and the bottom floor is.

3. Theoretical Calculation

3.1 Mechanical Analysis

The cross section of supporting beam parallel to XOZ is rectangular, so the inertia moment of supporting beam is [18]:

$$I = \frac{b_1 {h_1}^3}{12}, \tag{1}$$

where, b_1 and h_1 are respectively the width and thickness of supporting beam.

Under the acceleration a_Z along the axis Z, all parts of the structure move downward. The structure is symmetric about the center of the plane XOY, so it can be simplified into a model with two fixed ends. The fixed end of the supporting beam—denoted by the point "M" in Fig. 1(a)—is taken as the position 0 (where, $x_1 = 0$ in Eq. (2)), the deformation at the distance x_1 from the point "M" to the other fixed end—denoted by the point "N" in Fig. 1(a)—is $w(x_1)$.

According to the principle of mechanics, the relevant equations of deformation are as follows [19]:

$$EIw''(x_1) = Fx_1 - M_0, \tag{2}$$

$$F = \frac{(2m_1 + m_2 + m_3)a_Z}{2}, \tag{3}$$

where, F and M_0 are respectively, a supporting force and a constrained bending moment of the fixed end of supporting beam. m_1, m_2, and m_3 are respectively, the mass of the supporting beam, the mass of proof masses and the mass of the supporting frame. E is Young's modulus.

The boundary conditions for Eqs. (2) and (3) are

$$y(0) = 0, y'(0) = 0, y''(l_1) = 0, \tag{4}$$

where, l_1 is the length of the supporting beam.

The bending equation of the supporting beam can be expressed as

$$w_1(x_1) = \frac{F}{2EI}{x_1}^2(l_1 - \frac{2}{3}x_1), 0 \le x_1 \le l_1. \tag{5}$$

Now, "N" point is taken as 0 position (where, $x_2 = 0$ in Eq. (6)), the deformation at the distance x_2 from the point "N" to the inside edge of the mass—denoted by the point "K" in Fig. 1(a)—is $w_2(x_2)$, and the deformation of the end of the supporting beam is equal to the outer edge of the supporting frame

$$w_1(l_1) = w_2(0). \tag{6}$$

The bending equations of the supporting frame and proof masses can be expressed as

$$w_2(x_2) = \frac{(m_2+m_3)a_Z}{Ec_1{h_3}^3}(3{L_{NK}}^2 - {x_2}^2)x_2 + w_1(l_1), \quad 0 \le x_2 \le L_{NK}, \tag{7}$$

where, c_1 and c_2 are respectively, the outer width and inner width of the supporting frame; h_3 is thickness of the supporting frame; L_{NK} is the length between the point "N" and the point "K," which can be expressed as:

$$L_{NK} = l_3 + \frac{c_1 - c_2}{2}, \tag{8}$$

where, l_3 is width of the proof mass.

3.2 Calculation of Natural Frequency

According to Rayleigh-Ritz method, the natural frequency can be calculated [13,20]. The mode function of first order $Y(x)$ of the system is approximated:

$$Y(x) = y_0 \, sin\frac{2\pi}{L}x, \tag{9}$$

where, L is sensitive structure length. The boundary conditions for Eq. (7) are:

$$Y(0) = 0, \frac{d^2Y(0)}{dx^2} = 0, Y(L) = 0, \frac{d^2Y(L)}{dx^2} = 0\,. \tag{10}$$

The first natural frequency of the system can be calculated by the following equation:

$$\omega^2 = \frac{\int_0^L EI[Y''(x)]^2 dx}{\int_0^L Y^2(x)\frac{M}{L}dx} = \frac{\frac{1}{2}EI{y_0}^2L(\frac{2\pi}{L})^4}{{y_0}^2\frac{1}{2}M}, \tag{11}$$

where, M is the total mass of the accelerometer without regard to the accelerometer frame.

The natural frequency f can be obtained as

$$f = \pi\sqrt{\frac{Eb_1{h_1}^3}{3L^3M}}. \tag{12}$$

The mass of the sensing beams is four orders of magnitude less than that of other parts, so it is not included in the total mass. According to Eq. (12), the natural frequency is little affected by the size of the tiny sensing beam. In the formula, b_1 and h_1 are the size of the supporting beam; L is positively related to the length of the supporting beam l_1; and M is positively correlated with the length l_1, width b_1 and thickness h_1 of the supporting beam. Therefore, without changing the size of the proof masses, and without regard to the accelerometer frame, the natural frequency mainly depends on the size of the supporting beam, which can weaken the compromise between the natural frequency and the sensitivity.

3.3 Calculation of Damping Ratio

Damping has effects on the dynamic performance of the vibration system, such as linearity. In the accelerometer structure, the squeeze film effect arises from the interaction of the proof masses and the air film trapped between the bottom floor and the proof masses [20]. The damping ratio ξ of the accelerometer structure is

$$\xi = \frac{0.42\mu(2l_1+c_1){c_1}^3}{2\pi f(m_2+m_3)d^3}, \tag{13}$$

where, d is the distance between the proof masses and the bottom floor. μ is the air viscosity coefficient.

For the second order system, the system has the best dynamic performance when the damping ratio is 0.7 [20]. The damping ratio can be changed by adjusting the distance between the proof masses and the bottom floor. Through designing the bottom floor, the damping ratio can be adjusted to around 0.7.

4. Optimization Analysis

To avoid damage of the accelerometer structure caused by large deformation and high vibration when the accelerometer undergoes excessive impact, the structure needs further optimization. Firstly, four tiny sensing beams of size 40 μm×55 μm×10 μm and four proof masses of size 280 μm×280 μm×280 μm are designed. The size of the mass is far greater than that of the tiny sensing beam so that the accelerometer structure can be as sensitive as possible.

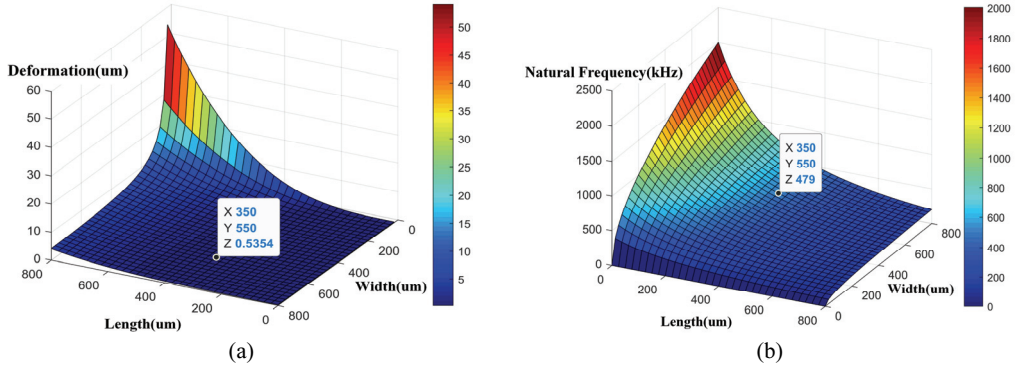

(a) (b)

Fig. 2. (a) Relationship between maximum deformation on surface and width/length of the supporting beam. (b) Relationship between natural frequency and width/length of the supporting beam.

Fig. 2 shows that shorter, wider supporting beams contribute to smaller deformation on surface and high natural frequency of the accelerometer, calculated by Eq. (7) and Eq. (10), respectively.

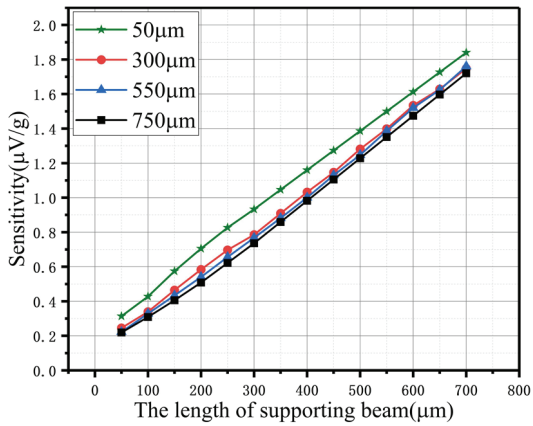

Fig. 3. The sensitivity of the accelerometer with different widths (50 μm, 300 μm, 550 μm, and 750 μm) and lengths of supporting beam.

The FEM analysis software ANSYS Workbench is used to build the preliminary model, mesh and simulate the structure of the accelerometer. The density of silicon material is 2,330 kg/m^3, Young's modulus is 1.7×10^{11} Pa [21]. Fig. 3 shows the results of sensitivity with different width and lengths of supporting beam, which shows that longer supporting beams can significantly improve sensitivity but the widths have a minor effect on sensitivity. Therefore, when sensitivity is also taken into account appropriately, the parameters of the accelerometer are showed in Table 1. When the distance between the proof masses and the bottom floor is 2.55 μm, the damping ratio can be close to 0.7.

Table 1. Structure parameters

	Parameter	Symbol	Value (mm)
Supporting beam	Length	l_1	350
	Width	b_1	550
	Height	h_1	100
Tiny sensing beam	Length	l_2	40
	Width	b_2	55
	Height	h_2	10
Mass	Length	l_3	280
	Height	h_3	200
Supporting frame	Outside length	c_1	800
	Inside length	c_2	600
	Height	h_4	110

5. Conclusion

5.1 Static Analysis

Under the acceleration from -220,000 g to 220,000 g along +Z axis, the results of maximum deforma-

tion and the maximum von-Mises stress are showed in Fig. 4 during the ±10% of measuring range of the accelerometer. The maximum deformation is 0.57 μm when external acceleration is 220,000 g, which is less than the distance between the proof masses and the bottom floor. The maximum von-Mises stress is 147.85 MPa when external acceleration is ±220,000 g, which is less than permissible stress of silicon [22]. So, the measuring range of the accelerometer can reach 200,000 g.

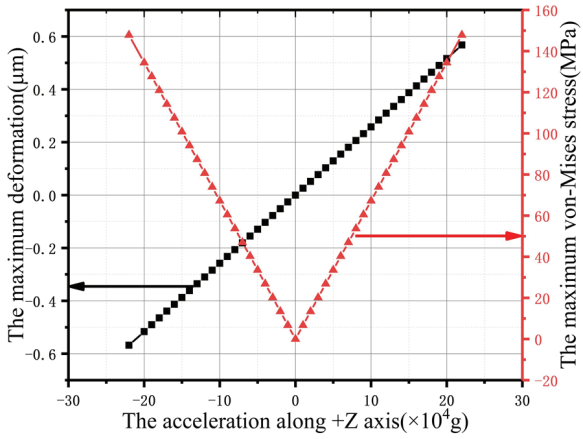

Fig. 4. The maximum deformation and the maximum von-Mises stress.

Under the acceleration of 200,000 g along the axis +Z, the theoretical results according to Eq. (7) and the simulation results of maximum deformation from the point "M" (0 μm of horizontal axis) to the point "K" (730 μm of horizontal axis) are show in Fig. 5.

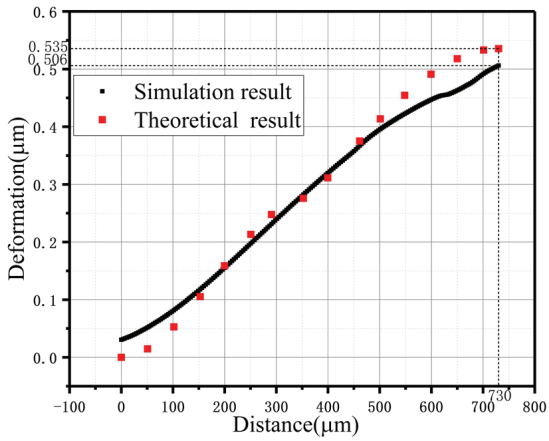

Fig. 5. Simulation and theoretical result of deformation from the point "M" to the point "K."

5.2 Sensitivity and Cross-Axis Sensitivity Analysis

Resistors are on the surface of tiny sensing beams. The lengths of four resistors are placed in the direction X ([110] crystal orientation of p-type silicon) [23], distributed on the central position of four tiny sensing beams, respectively (as shown in Fig. 6(a)). The size of the resistor is 40 μm×10 μm.

Wheatstone bridge circuit is adopted as the induction circuit of the accelerometer (as shown in Fig. 6(b)), with 5 V constant voltage source as the input signal U_{in}.

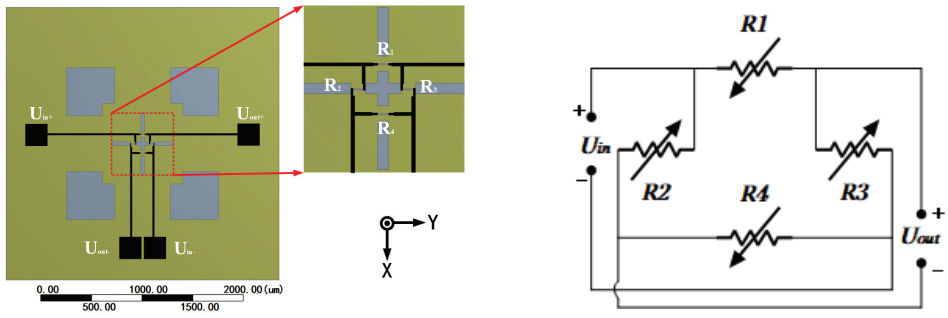

(a) (b)

Fig. 6. (a) Resistors distribution diagram and (b) Wheatstone bridge circuit.

When the accelerometer structure is not affected by acceleration, the tiny beams will not be out of shape. So, the resistance values of resistors will not change and be equal, and the Wheatstone bridge circuit has no output [24]. When the external acceleration input, the stress of R_1 and R_3 are equal, the stress of R_2 and R_4 are equal, so the output can be obtained by calculating the average stress of the resistors R_1 and R_2 [25].

$$U_{out} = \frac{\Delta R \cdot U_{in}}{R} = \frac{\pi_{44}}{2} \frac{(\sigma_{ZX1} - \sigma_{ZY1}) - (\sigma_{ZX2} - \sigma_{ZY2})}{2} \cdot U_{in}, \tag{14}$$

where, U_{out} and U_{in} are respectively, the output and input voltage of Wheatstone bridge circuit; σ_{ZX1} and σ_{ZX2}, respectively, represent the X-axis stress of the resistors R_1 and R_2, σ_{ZY1} and σ_{ZY2}, respectively represent the Y-axis stress of the resistors R_1 and R_2 when external acceleration is along Z-axis. π_{44} is a piezoresistive coefficient of p-type silicon at room temperature and the value is 138.1×10^{-11} m^2/N [26].

Different output under different acceleration can be calculated by Eq. (14) and the fitting result is in Fig. 8(c), so the sensitivity of the piezoresistive high-g accelerometer is 0.88 μV/g.

When external acceleration along the axis X, the sensitivity along the axis X (S_X) is as follows:

$$S_X = \frac{U_{out}}{a_X} = \frac{\Delta R \cdot U_{in}}{R \cdot a_X} = \frac{\pi_{44}}{2} \frac{(\sigma_{XY1} - \sigma_{XZ1}) - (\sigma_{XY2} - \sigma_{XZ2})}{2} \cdot \frac{U_{in}}{a_X}, \tag{15}$$

where, a_X is acceleration along the axis X;σ_{XY1}andσ_{XY2}respectively represent the Y-axis stress of the resistors R_1 and R_2, σ_{XZ1} and σ_{XZ2}, respectively, represent the Z-axis stress of the resistors R_1 and R_2 when external acceleration is along X-axis.

When external acceleration along the axis Y, the sensitivity along the axis Y (S_Y) is as follows:

$$S_Y = \frac{U_{out}}{a_Y} = \frac{\Delta R \cdot U_{in}}{R \cdot a_Y} = \frac{\pi_{44}}{2} \frac{(\sigma_{YX1} - \sigma_{YZ1}) - (\sigma_{YX2} - \sigma_{YZ2})}{2} \cdot \frac{U_{in}}{a_Y}, \tag{16}$$

where, a_Y is acceleration along the axis Y; σ_{YX1} and σ_{YX2}, respectively, represent the X-axis stress of the resistors R_1 and R_2, σ_{YZ1} and σ_{YZ2}, respectively, represent the Z-axis stress of the resistors$R_1$and$R_2$when

external acceleration is along Y-axis.

Cross-axis sensitivity is expressed by the ratio of the sensitivity of the axis X/Y to the sensitivity of the axis Z, so the cross-axis sensitivity of the axis X (S_{XZ}) and the cross-axis sensitivity of the axis Y (S_{YZ}) are as follows:

$$S_{XZ} = \frac{S_X}{S_Z} \times 100\%$$
$$S_{YZ} = \frac{S_Y}{S_Z} \times 100\% \tag{17}$$

Fig. 7 shows a common accelerometer structure for comparison. The sensitivity of the axis X, the axis Y and the axis Z of our proposed structure and this comparison structure are shown in Fig. 8.

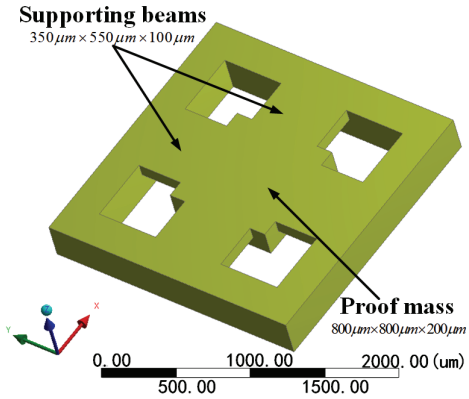

Fig. 7. The comparative accelerometer structure.

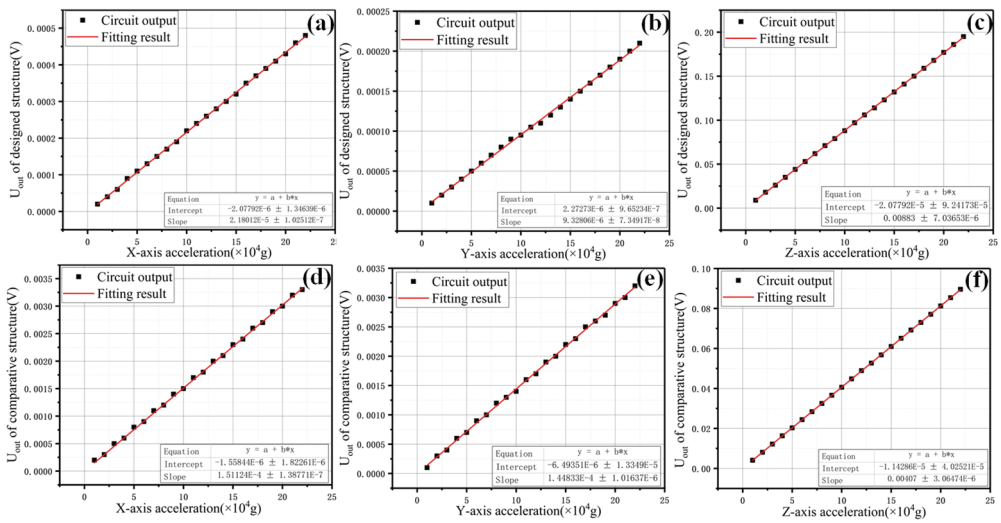

Fig. 8. The circuit output and fitting results. (a-c) The designed structure under X-axis, Y-axis, and Z-axis accelerations, respectively. (d-f) The comparative structure under X-axis, Y-axis, and Z-axis accelerations, respectively.

5.3 Model Analysis

Mechanical systems have many vibrating modes and corresponding resonant frequencies. By observing the vibrating modes and the resonant frequency of the structure through modal analysis, it is possible to predict whether the resonant frequency of the structure is suitable for high vibration conditions. The first order resonant frequency is natural frequency, other resonant frequencies are higher and higher, so the first to fourth order conditions are often considered for prediction of performance [15]. The design of the high-g accelerometer should have a high natural frequency. Other resonant frequencies should be much higher than the natural frequency, and the first order vibrating mode and second order vibrating mode should be different, so as to ensure that the designed high-g accelerometer can work normally in a vibration environment. In modal analysis, the end of the support beams is fixed, the first-four vibrating modes of the accelerometer sensitive structure are shown in Fig. 9, whose resonant frequencies are shown in Table 2.

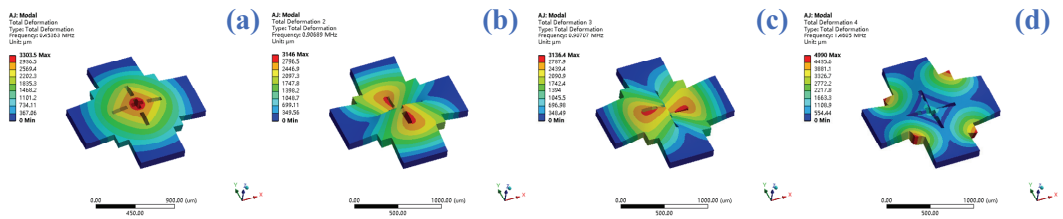

Fig. 9. The first-four order vibrating modes of the sensitive structure. (a) The first order vibrating mode is that the structure undulates along Z-axis, its resonant frequency is 453.6 kHz. (b) The second order vibrating mode is that the structure generates a vibration wave in the YOZ plane, its resonant frequency is 906.9 kHz. (c) The third order vibrating mode is that the structure generates a vibration wave in the XOZ plane, its resonant frequency is 907 kHz. (d) The fourth order vibrating mode is that the structure generates two vibration waves parallel to YOZ plane, its resonant frequency is 1460.5 kHz.

Table 2. First-four order resonant frequencies of the sensitive structure

	The first order	The second order	The third order	The fourth order
Resonant freq. (kHz)	453.6	906.9	907	1,460.5

In Fig. 9, the first order vibrating mode is characterized with the proof masses perpendicular to the XOY plane and reciprocating along the axis Z, which is the main mode with the natural frequency of 453.6 kHz. If the structure generates vibrations close to the natural frequency, the center of the structure (the red area in Fig. 9(a)) is most vulnerable. The second order and the third order vibrating mode have similar resonant shapes and resonant frequencies. Their resonant frequencies are more than twice of the natural frequency, which is conducive to reducing the mode interference [27]. Last, the fourth order vibrating mode is characterized with two proof masses on one side of the YOZ plane and two proof masses on the other side rotating clockwise and counterclockwise about the axis Y, respectively.

Fig. 10 shows the natural frequency with different widths and lengths of supporting beam, which is consistent with Eq. (12) that shorter and wider supporting beam can improve natural frequency. Since the length of the tiny sensing beam is equal to the width of the cross gap, and in order to avoid the

influence of the width of the tiny sensing beam on the position of the resistor, Fig. 11 shows that the thickness of tiny sensing beam has minor effect on natural frequency, which is consistent with Eq. (12), but thicker tiny sensing beam can improve sensitivity. So, combined with the results obtained in Section 4 that the width of supporting beam has minor effect on sensitivity, then the accelerometer structure can weaken the compromise between natural frequency and sensitivity.

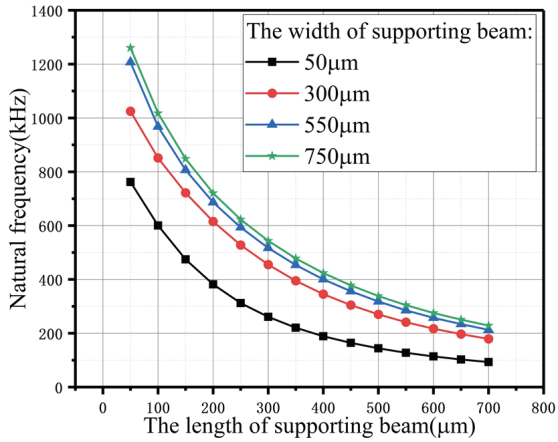

Fig. 10. Natural frequency with different lengths (50 μm, 300 μm, 550 μm, and 750 μm) and widths of supporting beam.

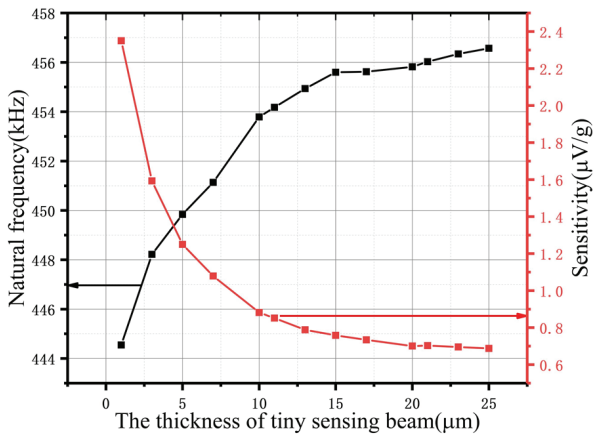

Fig. 11. Natural frequency and sensitivity with different thicknesses of the tiny sensing beam.

Fig. 11 shows the simulation and theoretical results of natural frequency with different widths of supporting beam. The theoretical results of natural frequency can be calculated according to Eq. (12). The simulation results agree with the theoretical ones with 5% bias, which is the average of biases per width sample—it is in total fourteen width samples in Fig. 12. The bias mainly comes from the deviation between the selected mode function and the actual mode function. Since Rayleigh method is an approximate estimation and simplifies the mode function to the expression of sine function, the selected mode function cannot be exactly the same as the actual mode function.

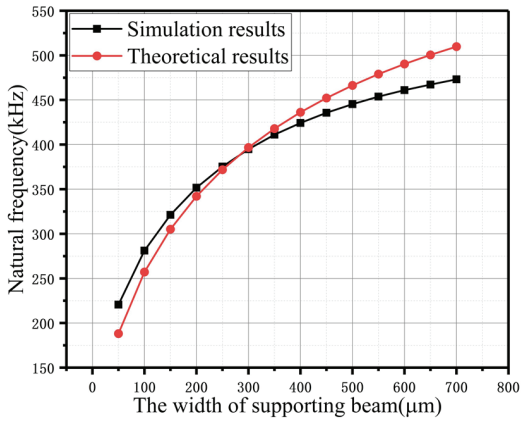

Fig. 12. Simulation and theoretical results of the natural frequency.

5.4 Impact Simulation

To test the dynamic characteristics of the accelerometer, we carry out an impact simulation. Ansys Workbench LS-DYNA is usually used to solve the time related problem, such as structural collision and impact [28].

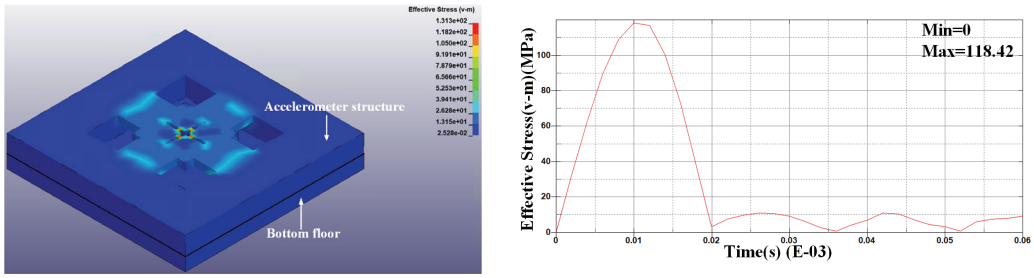

(a) (b)

Fig. 13. (a) Von-Mises stress of accelerometer surface while impact. (b) Von-Mises stress waveform of tiny sensing beam during 60 μs.

In LS-DYNA, 200,000 g impact is given to the accelerometer surface. The impact waveform is a half sine wave, whose duration is 20 μs. And observation time is 40 μs after impact. Fig. 13(a) shows that the stress mainly focused on the tiny sensing beams. Fig. 13(b) shows that the tiny sensing beams take 118.42 MPa impact, less than permissible stress of silicon. There is vibration after impact. The results show that the piezoresistive high-g accelerometer has strong resistance to impact.

5.5 Summary and Comparison

Table 3 summarizes the comparison of the proposed piezoresistive high-g accelerometer with existing devices [3,15,16,18,29]. The piezoresistive high-g accelerometer with the proposed structure has higher natural frequency and lower transverse effect. Only the structure is optimized, so this accelerometer can be produced by using silicon and basic processing. It is suitable for mass production. However, compared with triaxial accelerometers, there are some limitations when using proposed Z-aixs accelerometer. Using

three single-axis devices to measure three vectors may increase the volume and complexity of the measurement system.

Table 3. Performance comparisons with the existing devices

Structure	Sensitivity	Natural frequency	Transverse effect, X/Y (%)	Work axis	Materials
A single-cantilever structure and two dual-cantilever [3]	0.80–0.88 μV/g/5 V (X/Y), 1.36 μV/g/5 V (Z)	134.7 kHz	-	Three	Silicon
Eight supporting beams and four sensing beams [18]	4.15 μV/g/V	5,607 Hz	1.67/0.82	Single	Silicon
Our-beams and central-island mass [15]	0.5611 μV/g	408.19 kHz	-	Single	Silicon
Four self-supporting micro beams [16]	1.586 μV/g/3 V	445 kHz	-	Single	SOI
Eight beams (EBs) [29]	131.4 μV/g/V	14.8 kHz	1.04/0.76	Single	Silicon
Proof masses with a cross gap	0.88 μV/g/5 V	453.6 kHz	0.25/0.11	Single	Silicon

6. Conclusion

To improve natural frequency and to reduce transverse effect of piezoresistive high-g accelerometer, we introduce the design and simulation of a piezoresistive high-g accelerometer. Special-shaped proof masses system with a cross gap can shorten the distance between the gravity center of the proof system and the neutral layer of supporting beams to restrain the transverse effect. Four tiny sensing beams are bonded above the cross gap, which can weaken the compromise between natural frequency and sensitivity. The simulation results show that the natural frequency of the piezoresistive high-g accelerometer is 453.6 kHz and the sensitivity is 0.88 μV/g. The cross-axis sensitivity of the axis X axis and the axis Y is respectively, 0.25% and 0.11%. Contrastively, the cross-axis sensitivity of X-axis and Y-axis is respectively, reduced by 93.2% and 96.9%. It has a higher natural frequency and a lower transverse effect and the results of impact simulation meet the requirements. Our research provides a support for the application of design and fabrication of piezoresistive high-g accelerometers.

Acknowledgement

This paper is supported by Chongqing Natural Science Foundation of China (No. CSTC2021JCYJ-MSXMX0566).

References

[1] H. I. Jung, D. S. Kwon, and J. Kim, “Fabrication and characterization of monolithic piezoresistive high-g three-axis accelerometer,” *Micro and Nano Systems Letters*, vol. 5, article no. 7, 2017. https://doi.org/10.1186/s40486-016-0041-7

[2] P. Mohankumar, J. Ajayan, R. Yasodharan, P. Devendran, and R. Sambasivam, "A review of micromachined sensors for automotive applications," *Measurement*, vol. 140, pp. 305-322, 2019.

[3] S. Cai, W. Li, H. Zou, H. Bao, K. Zhang, J. Wang, Z. Song, and X. Li, "Design, fabrication, and testing of a monolithically integrated tri-axis high-shock accelerometer in single (111)-silicon wafer," *Micromachines*, vol. 10, no. 4, article no. 227, 2019. https://doi.org/10.3390/mi10040227

[4] X. Hu, P. Mackowiak, M. Bauscher, O. Ehrmann, K. D. Lang, M. Schneider-Ramelow, S. Linke, and H. D. Ngo, "Design and application of a high-G piezoresistive acceleration sensor for high-impact application," *Micromachines*, vol. 9, no. 6, article no. 266, 2018. https://doi.org/10.3390/mi9060266

[5] R. W. Zurek, R. H. Tolson, D. Baird, M. Z. Johnson, and S. W. Bougher, "Application of MAVEN accelerometer and attitude control data to Mars atmospheric characterization," *Space Science Reviews*, vol. 195, pp. 303-317, 2015.

[6] J. Wen, H. Yao, Z. Ji, B. Wu, and F. Xu, "Self-validating high-g accelerometers through data-driven methods," *Sensors and Actuators A: Physical*, vol. 328, article no. 112803, 2021. https://doi.org/10.1016/j.sna.2021.112803

[7] N. Gupta, S. Dutta, Y. Parmar, V. Gond, S. R. K. Vanjari, and S. Gupta, "Characterization of SOI MEMS capacitive accelerometer under varying acceleration shock pulse durations," *Microsystem Technologies*, vol. 27, no. 12, pp. 4319-4327, 2021.

[8] O. Paul, J. Gaspar, and P. Ruther, "Advanced silicon microstructures, sensors, and systems," *IEEJ Transactions on Electrical and Electronic Engineering*, vol. 2, no. 3, pp. 199-215, 2007.

[9] C. Jia, Q. Mao, S. Luo, L. Zhao, D. Lu, P. Yang, et al., "Novel high-performance piezoresistive shock accelerometer for ultra-high-g measurement utilizing self-support sensing beams," *Review of Scientific Instruments*, vol. 91, no. 8, article no. 085001, 2020. https://doi.org/10.1063/5.0008451

[10] J. Wen, H. Yao, Z. Ji, B. Wu, and M. Xia, "On fault diagnosis for high-g accelerometers via data-driven models," *IEEE Sensors Journal*, vol. 21, no. 2, pp. 1359-1368, 2021.

[11] H. Yao, J. Wen, Y. Ren, B. Wu, and Z. Ji, "Low-cost measurement of industrial shock signals via deep learning calibration," in *Proceedings of 2019 IEEE International Conference on Acoustics, Speech and Signal Processing (ICASSP)*, Brighton, UK, 2019, pp. 2892-2896.

[12] V. Narasimhan, H. Li, and J. Miao, "Micromachined high-g accelerometers: a review," *Journal of Micromechanics and Microengineering*, vol. 25, no. 3, article no. 033001, 2015. https://doi.org/10.1088/0960-1317/25/3/033001

[13] A. R. Atwell, R. S. Okojie, K. T. Kornegay, S. L. Roberson, and A. Beliveau, "Simulation, fabrication and testing of bulk micromachined 6H-SiC high-g piezoresistive accelerometers," *Sensors and Actuators A: Physical*, vol. 104, no. 1, pp. 11-18, 2003.

[14] Y. Shi, Y. Zhao, H. Feng, H. Cao, J. Tang, J. Li, R. Zhao, and J. Liu, "Design, fabrication and calibration of a high-G MEMS accelerometer," *Sensors and Actuators A: Physical*, vol. 279, pp. 733-742, 2018.

[15] Y. Shi, X. Wen, Y. Zhao, R. Zhao, H. Cao, and J. Liu, "Investigation and experiment of high shock packaging technology for high-g MEMS accelerometer," *IEEE Sensors Journal*, vol. 20, no. 16, pp. 9029-9037, 2020.

[16] C. Jia, L. Zhao, W. Jiang, X. Liu, M. Yu, M. Huang, Y. Xia, Y. Zhao, and Y. Zhao, "Impact experiment analysis of MEMS ultra-high G piezoresistive shock accelerometer," in *Proceedings of 2018 IEEE Micro Electro Mechanical Systems (MEMS)*, Belfast, UK, 2018, pp. 964-967.

[17] M. Jangra, D. S. Arya, R. Khosla, and S. K. Sharma, "Maskless lithography: an approach to SU-8 based sensitive and high-g Z-axis polymer MEMS accelerometer," *Microsystem Technologies*, vol. 27, no. 8, pp. 2925-2934, 2021.

[18] H. Han, Z. Zhao, W. Niu, R. Huang, and L. Dong, "A low cross-axis sensitivity piezoresistive accelerometer fabricated by masked-maskless wet etching," *Sensors and Actuators A: Physical*, vol. 283, pp. 17-25, 2018.

[19] M. Bao, *Analysis and Design Principles of MEMS Devices*. Amsterdam, The Netherlands: Elsevier, 2005.

[20] S. Biswas and A. K. Gogoi, "A wearable piezoresistive microaccelerometer with low cross-axis sensitivity for neurological disease diagnosis," *AEU-International Journal of Electronics and Communications*, vol. 99, pp. 177-185, 2019.

[21] M. A. Hopcroft, W. D. Nix, and T. W. Kenny, "What is the Young's modulus of silicon?," *Journal of Microelectromechanical Systems*, vol. 19, no. 2, pp. 229-238, 2010.

[22] C. J. Wilson and P. A. Beck, "Fracture testing of bulk silicon microcantilever beams subjected to a side load," *Journal of Microelectromechanical Systems*, vol. 5, no. 3, pp. 142-150, 1996.

[23] R. Kuells, S. Nau, M. Salk, and K. Thoma, "Novel piezoresistive high-g accelerometer geometry with very high sensitivity-bandwidth product," *Sensors and Actuators A: Physical*, vol. 182, pp. 41-48, 2012.

[24] Y. Wang, X. Zhao, and D. Wen, "Fabrication and characteristics of a three-axis accelerometer with double L-shaped beams," *Sensors*, vol. 20, no. 6, article no. 1780, 2020. https://doi.org/10.3390/s20061780

[25] Z. Ghemari and S. Saad, "Piezoresistive accelerometer mathematical model development with experimental validation," *IEEE Sensors Journal*, vol. 18, no. 7, pp. 2690-2696, 2018.

[26] A. A. Barlian, W. T. Park, J. R. Mallon, A. J. Rastegar, and B. L. Pruitt, "Semiconductor piezoresistance for microsystems," *Proceedings of the IEEE*, vol. 97, no. 3, pp. 513-552, 2009.

[27] Y. Zhao, X. Li, J. Liang, and Z. Jiang, "Design, fabrication and experiment of a MEMS piezoresistive high-g accelerometer," *Journal of Mechanical Science and Technology*, vol. 27, pp. 831-836, 2013.

[28] A. Garcia-Perez, F. Sorribes-Palmer, G. Alonso, and A. Ravanbakhsh, "Overview and application of FEM methods for shock analysis in space instruments," *Aerospace Science and Technology*, vol. 80, pp. 572-586, 2018.

[29] P. Wang, Y. Zhao, B. Tian, Y. Liu, Z. Wang, C. Li, and Y. Zhao, "A piezoresistive micro-accelerometer with high frequency response and low transverse effect," *Measurement Science and Technology*, vol. 28, article no. 015103, 2017. https://doi.org/10.1088/1361-6501/28/1/015103

Yongle Lu **https://orcid.org/0000-0002-0837-5793**

He received M.S. degree from Chongqing University of posts and telecommunications in 2012. He received the Ph.D. degree in instrument science and technology at Chongqing University in 2015. He is associate professor at Chongqing University of Posts and Telecommunications and a director of Chinese Institute of Inertial Technology. His research interests include solid state vibration gyro and photoelectric sensing technology.

Zhen Qu **https://orcid.org/0000-0002-1895-2988**

She received B.S. degree in integrated circuit from Huaqiao University in 2019. Since September 2019, she is purchasing M.S. degree in School of Optoelectronic Engineering of Chongqing University of Posts and Telecommunications. Her current research interest is inertial sensing technology.

Jie Yang **https://orcid.org/0000-0002-1420-2127**

He received B.S. degree in integrated circuit design and integrated system from Chongqing University of Posts and Telecommunications in 2021. Since September 2021, he is purchasing M.S. degree in School of Optoelectronic Engineering of Chongqing University of Posts and Telecommunications. His current research interests include inertial components and system, navigation and positioning.

Wenxin Wang **https://orcid.org/0000-0002-7497-7397**

He received B.S. degree in integrated circuit design and integrated system from Chongqing University of Posts and Telecommunications in 2019. Since September 2019, he is purchasing M.S. degree in School of Optoelectronic Engineering of Chongqing University of Posts and Telecommunications. His current research interests include inertial components and system, navigation and positioning.

Wenbo Wang **https://orcid.org/0000-0001-9001-2846**

He received B.S. degree in electronic science and technology from Chaohu college in 2018. Since September 2019, he is purchasing M.S. degree in School of Optoelectronic Engineering of Chongqing University of Posts and Telecommunications. His current research interests include quantum optics and optical fiber sensing.

Yu Liu **https://orcid.org/0000-0002-8555-5640**

He received M.S. and Ph.D. degrees in Chongqing University in 2000 and 2006, respectively. He is a professor and doctoral supervisor at Chongqing University of Posts and Telecommunications. He has been researching sensor parts and systems, motion detection, attitude measurement, navigation and positioning for a long time.